Nanoscale dynamics of Joule heating and bubble nucleation in a solid-state nanopore

Edlyn V. Levine, Michael M. Burns, and Jene A. Golovchenko

Nanoscale Dynamics of Joule heating and Bubble Nucleation in a Solid-State Nanopore

Edlyn V. Levine,[1] Michael M. Burns,[3] and Jene A. Golovchenko[1,2*]

[1]School of Engineering and Applied Sciences, Harvard University, Cambridge, MA 02138, USA

[2]Department of Physics, Harvard University, Cambridge, MA 02138, USA

[3]The Rowland Institute at Harvard, Cambridge, MA 02142, USA

*corresponding author. Phone: 617-495-3905; Fax: 617-496-0189; Email: golovchenko@physics.harvard.edu

We present a mathematical model for Joule heating of an electrolytic solution in a nanopore. The model couples the electrical and thermal dynamics responsible for rapid and extreme superheating of the electrolyte within the nanopore. The model is implemented numerically with a finite element calculation, yielding a time and spatially resolved temperature distribution in the nanopore region. Temperatures near the thermodynamic limit of superheat are predicted to be attained just before the explosive nucleation of a vapor bubble is observed experimentally. Knowledge of this temperature distribution enables the evaluation of related phenomena including bubble nucleation kinetics, relaxation oscillation, and bubble dynamics.

I. INTRODUCTION

This work treats the coupled electrical and thermal dynamics connected with the Joule heating of an electrolytic solution in a nanopore. This encompasses the related phenomena of vapor bubble nucleation, growth, and decay resulting from superheating of the solution above its boiling temperature at atmospheric pressure. This study was stimulated by recent experimental observations of superheating and homogeneous single bubble nucleation in a solid-state nanopore [1]. Understanding these dynamics is central to the problem of creating localized hot spots with high temperature gradients in confined aqueous solutions. This problem is of great importance to thermophoresis [2] and has proven challenging due to water's high thermal diffusivity [3]. Methods to generate and model localized hot spots have included previous work on Joule heating in micron sized holes [3], radiative heating of nanopores [4], heating by magnetic induction in micro/nanoparticles [5, 6] and heating by focused laser beams [7, 8].

In the experiments presented in [1], an ionic current is focused through a single nanopore in a thin insulating membrane immersed in an electrolyte. Voltage biased electrodes on either side of the

membrane produce a current that flows through the pore. On application of a step in the voltage bias, the measured conductance is observed to increase with time due to Joule heating of the electrolyte within the nanopore. For sufficiently large applied bias, a vapor bubble ultimately nucleates explosively at the center of the nanopore, and is observed optically, as well as by a rapid blockage of the pore current.

We have explored the complex physics involved by constructing a mathematical model of the inter-related electrical and thermal phenomena. We identify and evaluate the required materials properties, and implement a numerical, finite-element calculation to obtain solutions to the nonlinear equations governing the dynamics. Experimental determination of the spatial extent and temporal evolution of the temperature distribution within the pore are difficult. Therefore, we rely heavily on these model calculations to obtain a full understanding of the related experimentally observed phenomena including temperature dependent electrical conductivity, induced charge densities around the nanopore, bubble nucleation kinetics, bubble relaxation oscillation timescales, and bubble growth dynamics.

Related research concerning superheating and bubble nucleation in liquids has involved different heating methods, including pulse heating of a filament [9, 10], pool boiling [11], heating in a host liquid [12], micro-capillary boiling [13, 14], and laser induced heating of nanoparticles [15]. Comparative analysis is available in review articles [16-18] and texts [19-20]. The Joule heating of an electrolyte in a nanopore is a unique reproducible nanoscale platform with which to study non-equilibrium superheating and bubble nucleation on rapid time scales down to nanoseconds.

II. THE PHYSICS OF JOULE HEATING IN A NANOPORE

A. Governing Equations

The temperature dynamics for Joule heating of an electrolyte in a nanopore are governed by the heat equation with inclusion of a Joule heating source term

$$\rho C_p \frac{\partial}{\partial t} T(\boldsymbol{r}, t) = \nabla \cdot (\kappa \nabla T(\boldsymbol{r}, t)) + \boldsymbol{J}(\boldsymbol{r}, t) \cdot \boldsymbol{E}(\boldsymbol{r}, t) \tag{1}$$

T is the temperature, $\boldsymbol{J}$ is the current density, and $\boldsymbol{E}(\boldsymbol{r}, t) = -\nabla V(\boldsymbol{r}, t)$ is the electric field associated with an electrostatic potential $V(\boldsymbol{r}, t)$ in the quasi-static approximation. The material properties of density ρ, heat capacity C_p, and thermal conductivity κ are specific to each material of the nanopore system. These properties are dependent on the temperature of the liquid electrolyte, such that $\rho = \rho(T(\boldsymbol{r}, t))$, $C_p = C_p(T(\boldsymbol{r}, t))$, and $\kappa = \kappa(T(\boldsymbol{r}, t))$, and are approximated as constants for the solid membrane material. The

Joule heating source term $\boldsymbol{J} \cdot \boldsymbol{E}$, is only nonzero in the conducting electrolyte. The heat equation is coupled to the continuity equation

$$\nabla \cdot \boldsymbol{J} + \frac{\partial \rho_c}{\partial t} = 0 \tag{2}$$

where $\rho_c = \nabla \cdot (\epsilon \boldsymbol{E})$ is the charge density of ions in solution and ϵ is the electric permittivity of the electrolyte, also a function of temperature, $\epsilon = \epsilon(T(\boldsymbol{r}, t))$. The current density is related to the electric field by Ohm's law

$$\boldsymbol{J} = \sigma \boldsymbol{E} \tag{3}$$

where $\sigma = \sigma(T(\boldsymbol{r}, t))$ is the temperature-dependent electrical conductivity of the electrolyte. Current due to diffusion of ions is not included, and is discussed later in the text. Taken together, Eqns. (1) and (2) form a complete system of coupled differential equations for which the two scalar fields, $T(\boldsymbol{r}, t)$ and $V(\boldsymbol{r}, t)$, can be solved. The electric field, current density, and spatial dependence of material properties can all be subsequently calculated from these scalar fields.

B. Nanopore Geometry with Boundary & Initial Conditions

The experimental nanopore system being modeled consists of an insulating membrane of amorphous silicon nitride suspended on a silicon-dioxide—silicon frame, separating between two reservoirs of aqueous, 3M NaCl solution. Electrical contact between the two reservoirs is maintained by the presence of a single pore present in the membrane.

Finite element modeling allows for inclusion of the detailed geometric features of the nanopore system with dimensions taken from the experiments. Fig. 1 depicts a cross-section of the model geometry. The nanopore is slightly conical in shape due to the process of fabrication using ion beam sculpting [21]. The computational domain is half the size of the image in Fig. 1, taking advantage of the axial symmetry of the nanopore as labeled in the figure. All dimensions are given in Table I.

TABLE I. Dimension of the Nanopore System

	Thickness	Radial distance from $r = 0$
Si_3N_4 membrane	71nm	53.5nm[a]
SiO_2 layer	1.6μm	2.4μm
Si frame	54.74°[b]	53.12 μm

[a] This is the radius of the nanopore.
[b] This is the angle the Silicon makes with the layer of silicon-dioxide, labeled as θ in Fig. 1 from wet etching in KOH [22].

The initial condition for temperature is assumed everywhere to be equal to the ambient temperature measured at the time of the experiment, 293.15K. This temperature is imposed on the boundary of the domain, far from the nanopore. As shown in Fig. 1, the voltage V, is set to the experimental value on the lower boundary of the computational domain, and zero on the upper boundary, corresponding to electrodes. The boundary condition on the vertical boundary is zero normal current density J_n, as depicted in Fig. 1.

C. Material Properties

The values used for the properties of the membrane materials are reported in Table II. Using constant values is a reasonable approximation since the temperature of the membrane changes only slightly. In contrast, the material properties of the electrolyte must include their temperature dependence in order to accurately account for the effects of heating. However, material data for metastable superheated aqueous 3M NaCl solution at atmospheric pressure are not available for the extremely high temperature regime that is reached experimentally. Therefore, we use the values for ρ, C_p, and κ available from the IAPWS-95 formulation for the equation of state of water, shown in Fig. 2 [23-25]. Also shown is the temperature dependence of the dielectric, $\epsilon_r = \epsilon/\epsilon_0$, of water [26]. Experimental data for the solution's electrical conductivity at such high temperatures under atmospheric pressure are also not available. We address this by fitting the electrical conductivity to the experimentally measured conductance curves as discussed in the results.

TABLE II. Material Properties of the Membrane[a]

	ρ [kg/m³]	C_p [J/(kg*K)]	κ [W/(m*K)]	σ [S/m]	ϵ_r
Si₃N₄ membrane	3100	700	3.2[b]	0	9.7
SiO₂ layer	2200	730	1.4[c]	0	4.2
Si frame	2329	700	130	10	11.7

[a] Data from COMSOL material library, unless otherwise indicated
[b] Thermal conductivity is for LPCVD silicon nitride films [27, 28]
[c] Thermal conductivity of silicon-dioxide thin films [29]

D. Numerical Implementation

The system of governing equations was solved using the commercial finite element software COMSOL 5.0 (Comsol, Inc.), with the geometry and materials of the nanopore system. The model geometry, depicted in Fig. 1, was chosen to be two-dimensional, and axisymmetric along the axis through the pore center. This drastically reduces the computational domain of the problem from that of a fully three

dimensional model. The modeled domain extends 100 μm from the nanopore. This distance is sufficiently large such that the room temperature boundary condition does not impact the solution anywhere in the domain.

Mesh resolution and time stepping were adjusted such that no variation in the solution occurred with changing of the spatial and time discretization parameters. A fine triangular mesh was required in the neighborhood of the nanopore due to its small dimension. Mesh elements in and around the nanopore had a width on the order of a nanometer. The mesh element size was scaled up for regions of the domain far away from the pore, reflecting the small variation of the fields being solved and the courser geometrical features in that region of the domain. An initial time step of 10^{-5} ns was used to initiate the time dependent calculation, with a maximum time step of 10^2 ns.

A time-dependent study modeled the dynamics of heating. The calculation is started just after a voltage pulse is turned on at $t = 0$. The electrical potential, $V(\boldsymbol{r}, 0)$, everywhere in the domain was calculated using COMSOL's Electric Currents (ec) module. This module solves the steady-state form of Eqn. 2, along with Eqn. 3 by implementing an affine invariant form of the damped Newton method [30]. The result of this calculation was then used as the initial condition in the time-dependent study of the Joule Heating (jh) module. This module solves the coupled system of equations, Eqns. (1-3) using variable-order, variable-step-size backward differentiation formulas [31].

III. RESULTS AND DISCUSSION

A. Conductivity of the Superheated Electrolyte

Calculating the dynamics of nanopore heating requires ascertaining the temperature dependence of the electrical conductivity $\sigma(T)$ of the aqueous 3M NaCl solution at atmospheric pressure. The temperature distribution $(\boldsymbol{r}, t)$, in the nanopore there leads to a spatially varying electrical conductivity $\sigma(T(\boldsymbol{r}, t))$. In Fig. 3(a), we show conductivity data taken of a bulk sample of 3M NaCl solution for $T < 373$K at atmospheric pressure. Above this temperature and pressure, the bulk sample boils, rendering further data acquisition difficult. However, we are able to determine an appropriate form $\sigma(T)$ by fitting the experimentally measured nanopore conductance curves for the case in which the solution does superheat. These data were obtained by applying voltage pulses ranging from 4 to 8.22V across a 53.5nm radius, 71 nm thick nanopore [1]. $\sigma(T)$ is assumed to take the form

$$\sigma(T) = mT - b - \frac{(T-T_0)^\alpha}{\beta} \tag{4}$$

with $T_0 = 293.15$K. The linear trend for $T < 373$K is expressed by the first two terms on the right hand side. The constants m and b were determined by fitting the bulk solution conductivity data of Fig. 3(a), and are equal to 0.391 ± 0.002 S/(m K) and 96.9 ± 0.06 S/m respectively. The third term on the right hand side is a corrective factor accounting for the high temperature behavior of $\sigma(T)$ beyond the boiling point. The parameters α and β were treated as free parameters in calculations to fit the shape of the measured time-dependent nanopore conductance, $G(t)$ plotted in Fig. 3(b). The conductance is the result of the surface integral

$$G(t) = \int \sigma(T(\boldsymbol{r}, t))d^2r \tag{5}$$

over the cross sectional area of the nanopore. Fitted values of $\alpha = 2.7\pm0.01$ and $\beta = 5.6\times10^4 \pm 0.1\times10^4$ resulted in the computed pore conductance curves shown in Fig. 3(b). A plot of $\sigma(T)$ with these parameter values is shown in Fig. 3(a) in comparison with our measured conductivity as well as data collected by Bannard at higher pressures [32]. It is evident that in the superheated temperature regime, the electrical conductivity of aqueous NaCl solution ultimately starts to decrease with increasing temperature. This is an expected consequence of decreasing density and dielectric constant of water with increasing temperature [32, 33].

B. Extreme Superheating within the Nanopore

The calculated temperature attained at the pore center after 10μs for each applied voltage is indicated for each conductance trace in Fig. 3(b). Fig. 4 shows the contour plots of the temperature field within the nanopore at 10.4 μs for 4 V, 5 V, 6 V, 7 V, and 8.22 V applied. In the case of 8.22 V, extreme superheating is calculated to occur, strongly localized at the pore center. A maximum of 603 K is obtained at the center of the pore, dropping by 130 K to the edge of the pore, 53.5 nm from the center. The maximum temperature is about 5% greater than the theoretical limit of pure water [16]. The high concentration of NaCl in solution may contribute to this increase in a manner similar to boiling point elevation in electrolyte solutions [34].

It is evident from the temperature contour that the region of superheated liquid extends to 230nm from the pore center. The amount of stored thermal energy available for bubble formation and expansion in this superheated region is approximately 5pJ. This is determined by integrating

$$\varepsilon = \int C_p(T(\boldsymbol{r}))\rho_L(T(\boldsymbol{r}))(T(\boldsymbol{r}) - T_b)d^3r \tag{6}$$

6

where $T(r)$ is the temperature distribution at 10.4µs, and T_b is the boiling temperature at atmospheric pressure. The integration domain is defined by the region for which $T(r) > T_b$. The upper limit for the radius of a spherical bubble corresponding to this energy is 620 nm, accounting for latent heat of vaporization and assuming no thermal losses due to thermal diffusion.

C. Induced Charge Densities Near the Nanopore

The sharply peaked temperature distribution in the region of the nanopore results in a spatially dependent electrical conductivity σ, and electrical permittivity ϵ. The non-zero gradients of these material properties result in induced charge densities consistent with $\nabla \cdot J = 0$. This is evident upon inserting Eqn. (3), giving

$$\nabla \cdot J = \nabla\sigma \cdot E + \sigma\nabla \cdot E = 0 \tag{7}$$

This shows that divergence of the electric field in the neighborhood of the nanopore is not zero due to the non-zero gradient in the electrical conductivity. We can further solve for the free charge density, ρ_c

$$\epsilon_0 \nabla \cdot E = \rho_c + \rho_{pol} \tag{8}$$

where ρ_{pol} is the polarization charge density. Using Eqn. (3), and $\rho_{pol} = -\nabla \cdot (\epsilon_0 \chi_e E)$ we can solve for the free charge density in terms of the current density

$$\rho_c = \frac{\epsilon}{\sigma}\left(\frac{\nabla\epsilon}{\epsilon} - \frac{\nabla\sigma}{\sigma}\right) \cdot J \tag{9}$$

where the electrical susceptibility χ_e, has been written in terms of the ϵ, by the relation $\epsilon = \epsilon_0(1 + \chi_e)$. The variation of the conductivity of the material, expressed in the second term on the right hand side, allows for charging of the spatially varying dielectric in the first term, such that a net free charge density results. Fig. 5 shows the calculated free charge density and polarization charge density plotted along the central axis of the nanopore. The polarization charge density is seen to only be partially screened by the free charge, leading to a total, non-zero charge density near the pore.

It is important to note that this treatment is approximate since it does not include the diffusive current resulting from the gradient in density of the free charge carriers. This diffusive current will act to reduce the build-up of charge reported in Fig. 5. However, since this density is very small, with a maximum corresponding to 4×10^{-4} M, the inclusion of the diffusive term would be a correction to what is already a minor effect.

D. Nucleation of a Vapor Bubble

The magnitude of the localized temperature maximum calculated within the pore drastically increases the probability that a vapor bubble will nucleate homogeneously there. Experimentally, this nucleation event is observed optically, as well as in the rapid drop in the pore current as the nucleated bubble grows to block the ionic current through the pore [1]. Fig. 6(a) shows a continuation of the 8.22V conductance data plotted in Fig. 3(b) with an initial nucleation event occurring at 10.4μs. Subsequent nucleation events occur quasi-periodically thereafter. The nucleation of a vapor bubble at a given time and location within the nanopore requires extremely high temperatures to be attained. In Fig. 6(b), we plot the maximum calculated temperature as a function of time for each of the applied voltages. In order to quantify the likelihood of an initial nucleation event occurring at the pore center for 8.22 V applied, we calculate the nucleation rate $\mathcal{J}$, as a function of distance from the center of the nanopore. From classical nucleation theory [18], the nucleation rate gives the number of nucleation events that occur per unit volume per unit time

$$\mathcal{J}(T) = \frac{\rho_L}{m}\sqrt{\frac{3\gamma}{\pi m}}\exp\left[-\frac{16\pi\gamma^3}{3k_B T(P_e - P_\infty)^2\delta^2}\right] \tag{10}$$

where γ is the surface tension of the liquid-vapor interface, P_e is the equilibrium vapor pressure, P_∞ is the ambient pressure of 1 atm, and m is the mass of a single water molecule. Both γ and P_e are temperature-dependent. The factor δ is a correction factor required for using the equilibrium vapor pressure rather than the vapor pressure inside the bubble. This can be shown to be [18]

$$\delta = 1 - \frac{\rho_V}{\rho_L} + \frac{1}{2}\left(\frac{\rho_V}{\rho_L}\right)^{1/2} \tag{11}$$

where ρ_V is the temperature-dependent density of the vapor in the bubble.

Using the computed temperature distribution $T(r)$ in Eqn. (10) we plot the nucleation rate as a function of the distance from the center of the nanopore shown in Fig. 6(c), for times 8 μs, 9 μs, 10 μs, and 10.4 μs. The nucleation rate proves to be exquisitely sensitive to the temperature of the solution due to the strong temperature-dependence of the exponential factor in Eqn. (10). This dependence results from the decrease of γ with increasing temperature, shown in the inset of Fig. 6(c), as well as the increase of P_e with increasing temperature. Together, these cause the exponential of Eqn. (10) to grow as temperature rises. At temperatures approaching the limit of superheat, $\mathcal{J}$ increases by as much as two orders of magnitude per degree kelvin increase. This results in extreme focusing of the nucleation rate at the center of the pore where the solution is hottest, and occurs rapidly over only a few microseconds. Fig. 6(d) shows this explicitly by plotting the maximum nucleation rate as a function of time for 8.22 V, calculated from the

curve in Fig. 6(b). The inset of Fig. 6(d) shows the dependence $J(T)$ from Eqn. (9) indicating that the nucleation rate is negligible for the cases with applied voltage smaller than 8.22 V. The nucleation rate is only non-negligible after 8 μs and is localized to within 10nm of the pore center, verifying the experimental observation that homogeneous nucleation occurs there [1].

E. Dynamics of Heating and Relaxation Oscillation

The conductance trace in Fig. 6(a) shows that nucleation events occur quasi-periodically after the initial bubble nucleates. This behavior is that of a relaxation oscillator whose periodicity can be understood from the finite element calculation of the heating dynamics. A plot of the maximum temperature as a function of time is shown in Fig. 7(a). For this calculation, an applied voltage of 8.22V is turned on at $t = 0$, shut off for 16 ns at $t = 10.4$ μs, and then switched back on at $t = 10.416$ μs. The 16 ns over which the voltage is switched off approximates the 16ns lifetime of the bubble measured experimentally. During this time, the maximum temperature drops by 180K, plotted in Fig. 7(a). This rapid fall can be understood by the extreme temperature gradient driving thermal diffusion cooling. Fig. 7(b) shows a plot of the temperature distribution at different times along the cut-line of arrow shown in the inset. At 10.4 μs the temperature is extremely peaked, and is seen to drop rapidly for each increment of 4 ns. At 10.416 μs, the temperature at the pore center is still largely superheated, but the strong peak has dissipated. The amount of thermal energy that remains at 10.416 μs explains why reheating can occur so rapidly. As seen in Fig. 7(a), once the voltage is turned back on, the maximum temperature is largely recovered within approximately 100ns. The total blockage time and reheating time corresponds well to the experimentally measured time to the second bubble of 117 ns labeled in Fig. 6(a).

F. Initial Growth of the Bubble

The bubble blockage time of 16 ns can only be understood by full hydrodynamic modeling of the bubble dynamics. This treatment is beyond the scope of this paper. However, it is possible to understand the conductance fall time of 1 ns labeled in Fig. 6(a) from Rayliegh-Plesset theory for the growth of a spherical bubble in superheated liquid [35-37]. The equation describing the time-dependent, radial growth, $R(t)$ of a spherical bubble with initial radius R_0 and internal pressure P_V is

$$R(t)\ddot{R}(t) + \frac{3}{2}\dot{R}(t)^2 = \frac{P_V - P_\infty}{\rho_L} - 4\nu\frac{\dot{R}(t)}{R(t)} + \frac{2\gamma}{\rho_L R(t)} \tag{12}$$

where ν is the viscosity of the liquid and P_∞ is again 1 atm. We assign constant values of $P_V = 1.3\times10^7$ Pa, $\rho_L = 640$ kg/m³, $\nu = 1.2\times10^{-7}$ m²/s, and $\gamma = 0.008$N/m corresponding to liquid-vapor saturation of

9

water at 603K [38]. R_0 is assumed to be slightly larger than the critical bubble radius at 603K. The critical radius, given by the Laplace Pressure

$$R_c = \frac{2\gamma}{P_V - P_\infty}$$ (13)

is the minimum possible radius required for a nucleated bubble to grow equal to 1.2 nm at 603K. R_c represents mechanical equilibrium of Eqn. (12); therefore, we assume $R_0 = R_c + \epsilon$, where ϵ is a small perturbation factor equal to 0.1 nm.

The resulting time dependence of $R(t)$ is plotted in Fig. 8, showing the bubble radius reaching the pore wall in 0.6ns with an average velocity over this time of 90m/s. This corresponds well with measured 50m/s bubble growth velocity reported in our previous work [1].

It is important to note that the Rayleigh-Plesset growth modeling does not include mass transfer at the boundary or heat transport effects. At high temperature, the surface tension is greatly diminished, decreasing its effect on early growth. The effects of heat transport are only manifest in later stages of bubble growth [35]. A comprehensive analysis of the bubble dynamics over its lifetime requires the time evolution of heat transport and pressure in the bubble with a moving boundary condition.

IV. CONCLUSION

We have previously demonstrated that Joule heating in nanopores is a unique experimental platform to investigate extreme superheating and homogeneous vapor bubble nucleation. In this work, we presented the theory and calculations elucidating this phenomenon. Most importantly we report the calculated spatial and temporal temperature distribution in the electrolyte within the nanopore. The extreme, highly localized temperature distribution explains the unique properties of Joule heating in nanopores. These include the possibility of non-zero local charge density, the kinetics of homogeneous single-bubble nucleation, and the quasiperiodic nature of nucleation events in the nanopore. A complete understanding of controlled superheating and bubble nucleation in nanopores opens the possibility for developing applications of this system in chemistry and microfluidics.

REFERENCES

[1]   G. Nagashima, E. V. Levine, D. P. Hoogerheide, M. M. Burns, and J. A. Golovchenko, Phys. Rev. Lett. **113**, 024506 (2014).

[2]   S. Duhr, and D. Braun, Proc. Natl. Acad. Sci. U. S. A. **103**, 19678 (2006).

[3]   V. Viasnoff, U. Bockelmann, A. Meller, H. Isambert, L. Laufer, and Y. Tsori, Appl. Phys. Lett. **96**, 163701 (2010).

[4]   M. Belkin, C. Maffeo, D. B. Wells, and A. Aksimentiev, ACS Nano, **7**, 6816 (2013).

[5]   K. Hamad-Schifferli, J. J. Schwartz, A. T. Santos, S. Zhang, and J. M. Jacobson, Nature, **415**, 152 (2002).

[6]   M. Lévy, C. Wilhelm, J.-M. Siaugue, O. Horner, J.-C. Bacri, and F. Gazeau, J. Phys. Condens. Matter, **20**, 204133 (2008).

[7]   P. Baaske, S. Duhr, and D. Braun, Appl. Phys. Lett., **91**, 13 (2007).

[8]   D. Braun and A. Libchaber, Phys. Rev. Lett., **89**, 188103 (2002).

[9]   S. Glod, D. Poulikakos, Z. Zhao, and G. Yadigaroglu, Int. J. Heat Mass Tran. **45,** 367 (2002).

[10]   K. Derewnicki, Int. J. Heat Mass Tran. **28**, 2085 (1985).

[11]   X. Xu and T. Qian, Phys. Rev. E **89**, 063002, 2014.

[12]   R. E. Apfel, Nat. Phys. Sci. **238**, 63 (1972).

[13]   J. Li and P. Cheng, Int. J. Heat Mass Tran. **47**, 2689 (2004).

[14]   J. Thome, Int. J. Heat Fluid Fl. **25,** 128 (2004).

[15]   A. Kotaidis and A. Plech, App. Phys. Lett. **87**, 213102 (2005).

[16]   F. Caupin and E. Herbert, CR Phys. **7**, 1000 (2006).

[17]   C. T. Avedisian, J. Phys. Chem. Ref. Data **14**, 695 (1985).

[18]   M. Blander and J. L. Katz, AIChE J. **21**, 833 (1975).

[19]   P. G. Debenedetti, *Metastable Liquids: Concepts and Principles* (Princeton University Press, Princeton, 1996).

[20]   V. P. Skripov, *Metastable Liquids* (Wiley, New York, 1974).

[21]   J. Li, D. Stein, C. McMullan, D. Branton, M. J. Aziz, and J. A. Golovchenko, Nature **412**, 166 (2001).

[22]   K. E. Bean, IEEE Transactions on Electron Devices, **25**, 1185 (1978).

[23]   W. Wagner and A. Pruß, J. Phys. Chem. Ref. Data **31**, 387 (2002).

[24]   *Revised Release on the IAPWS Formulation 1995 for the Thermodynamic Properties of Ordinary Water Substance for General and Scientific Use*, (The International Association for the Properties of Water and Steam, Doorwerth, The Netherlands, September, 2009, http://www.iapws.org/relguide/IAPWS-95.html).

[25]   *Release on the IAPWS Formulation 2011 for the Thermal Conductivity of Ordinary Water Substance* (The International Association for the Properties of Water and Steam, Plzen, Czech Republic, pp. 1−15, September, 2011, http://www.iapws.org/relguide/ThCond.html).

[26]   A. S. Quist and W. L. Marshall, J. Phys. Chem., **69**, 3165 (1965).

[27]   X. Zhang and C. P. Grigoropoulosa, Rev. Sci. Instrum. **66**, 1115 (1995).

[28]   R. Sultan, A. D. Avery, G. Stiehl, and B. L. Zink, J. Appl. Phys. **105**, 043501 (2009).

[29]   T. Yamane, N. Nagai, S. Katayama, and M. Todoki, J. Appl. Phys. **91**, 9772 (2002).

[30]   P. Deuflhard, *Numer. Math.*, **22**, 289 (1974).

[31]   A.C. Hindmarsh, P.N. Brown, K.E. Grant, S.L. Lee, R. Serban, D.E. Shumaker, and C.S. Woodward, ACM T. Math. Software, **31**, 363, (2005).

[32]   J. Bannard, J. Appl. Electrochem. **5**, 43 (1975).

[33]   A. S. Quist and W. L. Marshall, J. Phys. Chem. **72**, 684 (1968).

[34]   T. Driesner, C. A. Heinrich, Geochim. Cosmochim. Acta **71**, 4880 (2007).

[35]   H. Lee and H. Merte, Jr., Int. J. Heat Mass Tran. **39**, 2427 (1996).

[36]   A. Prosperetti and M. S. Plesset, J. Fluid Mech. **85**, 349 (1978).

[37]   C. E. Brennen, *Cavitation and Bubble Dynamics*, (Cambridge, New York, 2014).

[38]   E.W. Lemmon, M.O. McLinden and D.G. Friend, *NIST Chemistry WebBook*, *NIST Standard Reference Database Number 69* (Eds. P.J. Linstrom and W.G. Mallard, National Institute of Standards and Technology, Gaithersburgh MD, retrieved March 2014, http://webbook.nist.gov)
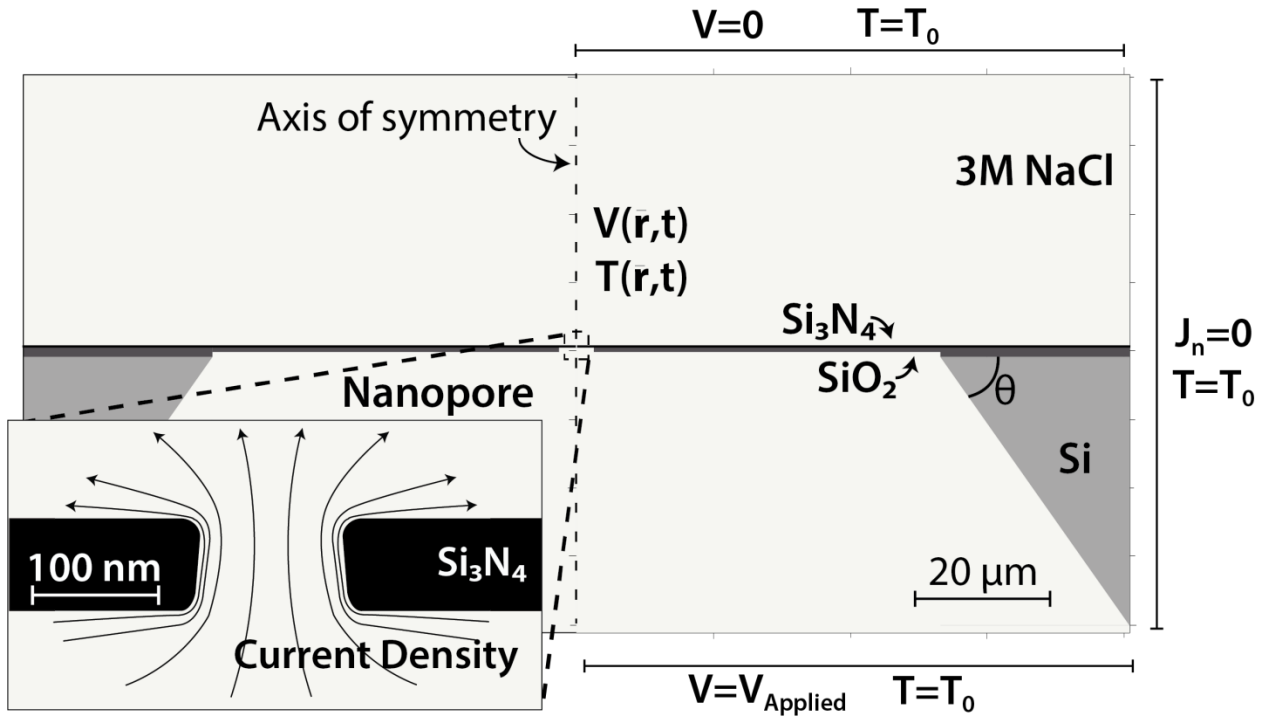
FIG. 1 Schematic of the nanopore system. A two-dimensional axi-symmetric model of the system was developed. The axis of symmetry is shown down the center of the model, with boundary conditions indicated on the edges of the computational domain with T_0 =273.15K. For clarity, the system is reflected across the axis of symmetry, and an inset shows the dimension of the nanopore to scale.

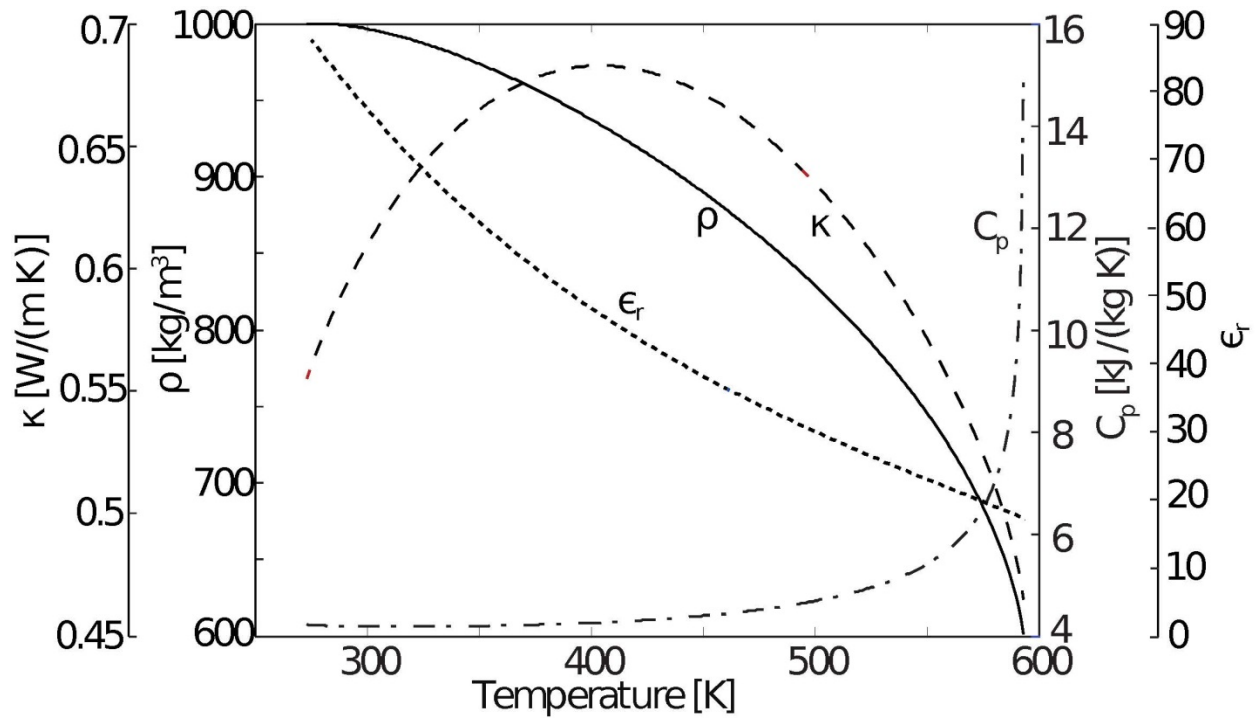FIG. 2 Temperature dependence of the material properties of water. The density ρ, thermal conductivity κ, and heat capacity C_p, are calculated from the IAPWS equation of state for superheated water at 1 atm [23-25]. The electrical permittivity $\epsilon_r = \epsilon/\epsilon_0$ is saturation curve data for water [26].
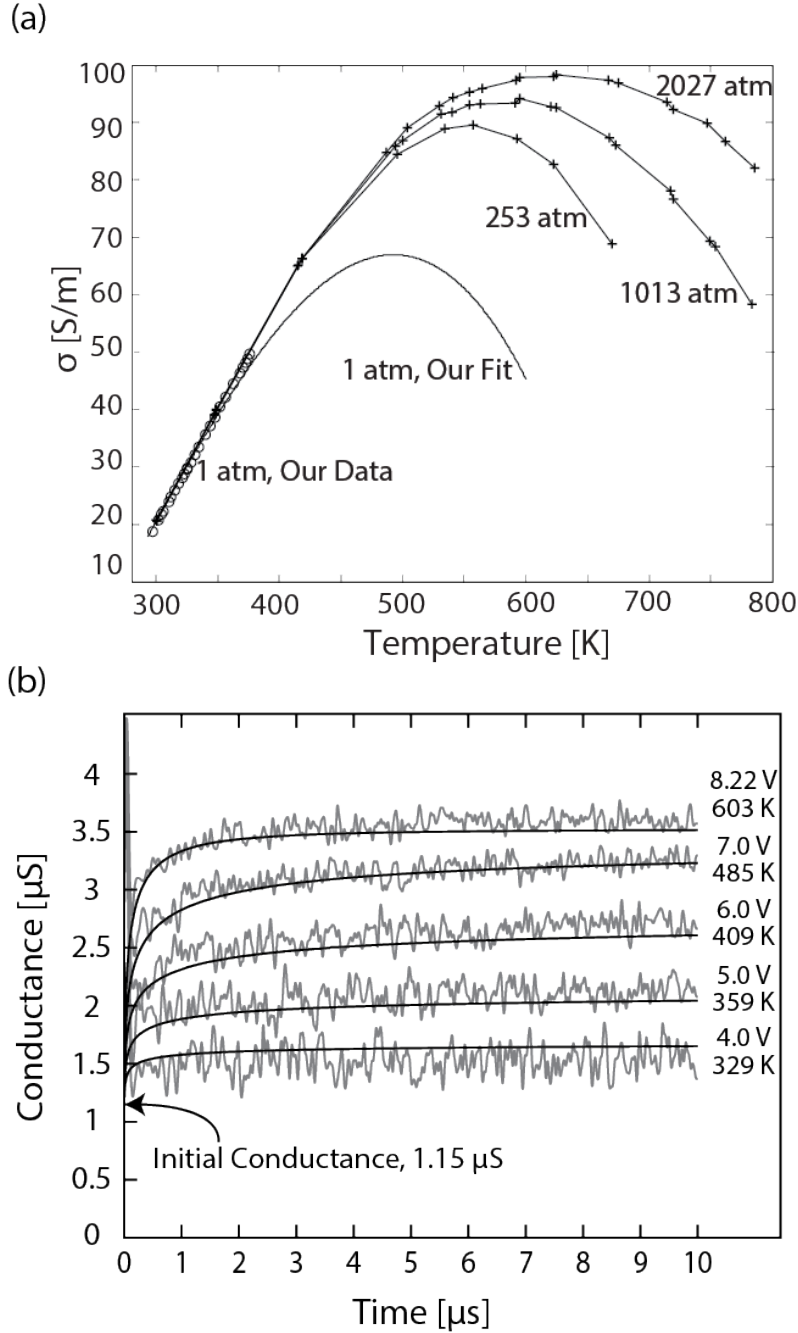
FIG. 3 (a) The temperature-dependent behavior of the conductivity of aqueous 3M NaCl solution. We calculated our fit for $\sigma(T)$ at 1atm using our own data for bulk conductivity measured below 373K, and by comparing to conductivity measurements taken at much higher pressures by Bannard [32]. (b) Data for the measured nanopore conductance traces taken for different applied voltages are shown with the calculated conductance curves [1]. The predicted peak temperature obtained within the nanopore is reported for each curve.
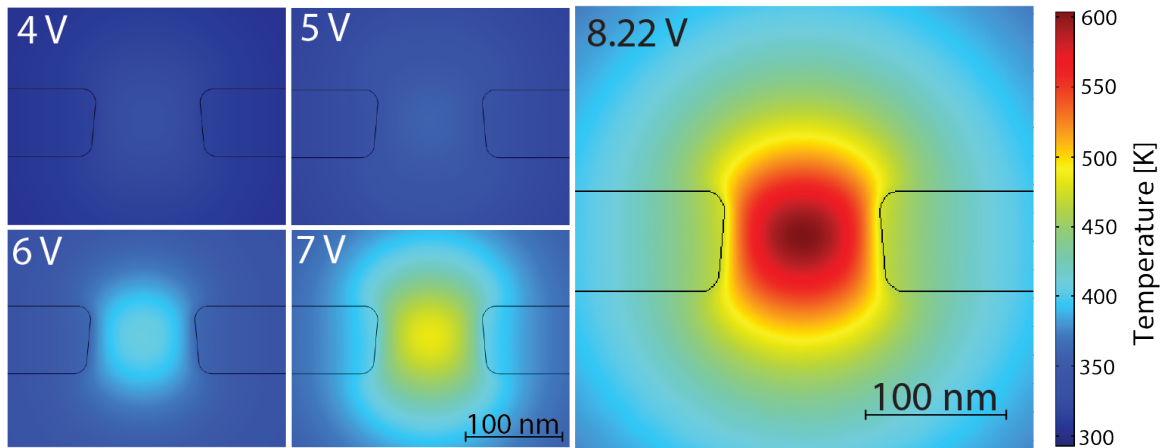
FIG. 4 (color). Contour plots showing the calculated temperature distribution in the nanopore after application of a 4V, 5V, 6V, 7V and 8.22V pulse for 10.4μs.
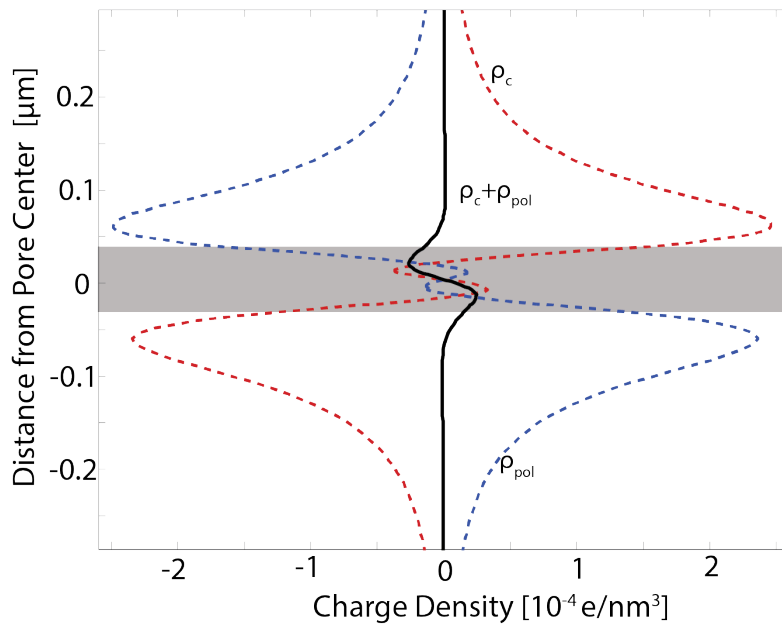

FIG. 5 (color). The calculated free charge density ρ_c, and polarization charge density ρ_{pol} plotted along the central axis of the nanopore. The total charge density $\rho_c + \rho_{pol}$ is also plotted and is nonzero in the region of the nanopore. The grey band indicates the location of the nanopore.
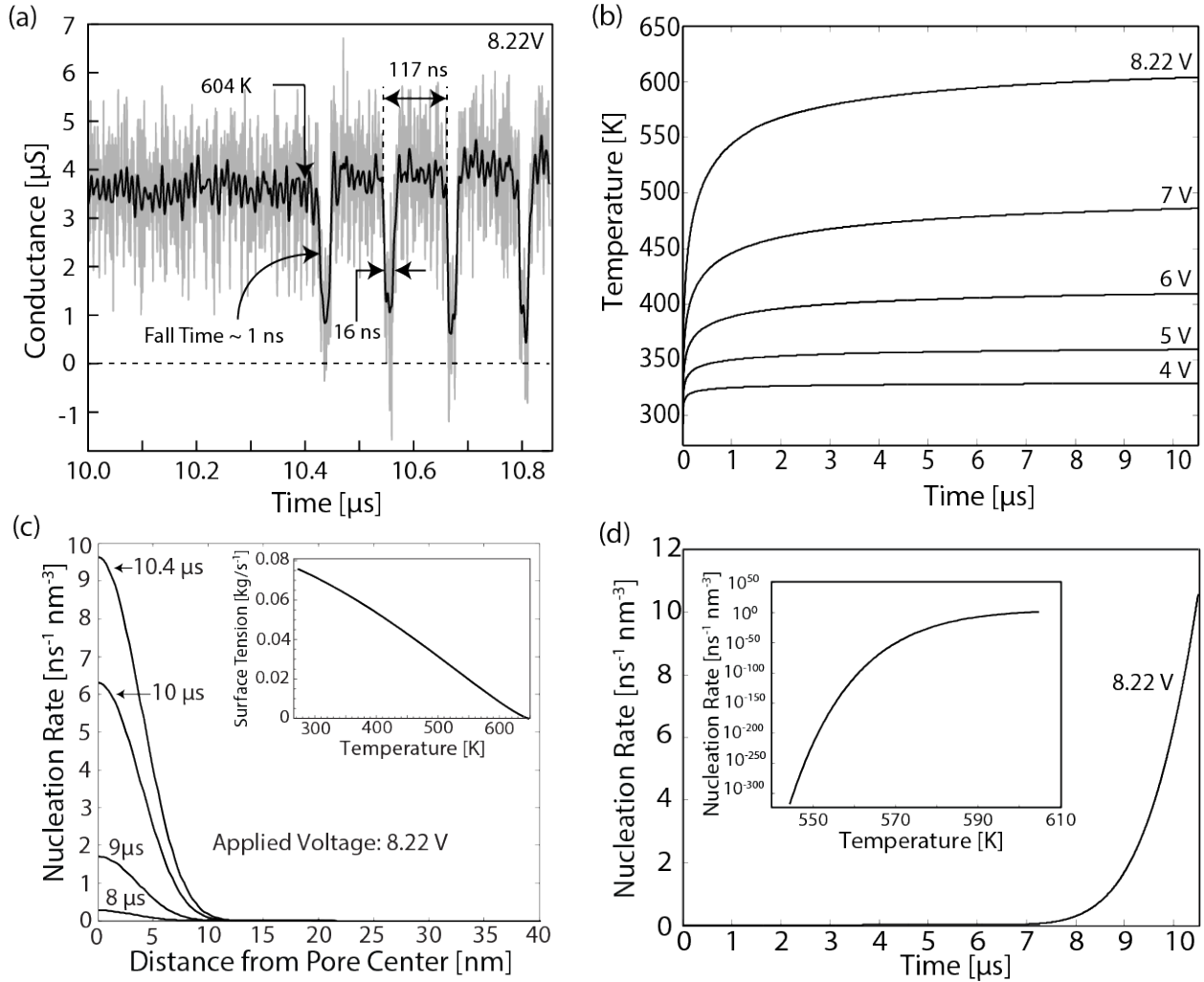
FIG. 6 (a) A continuation of the conductance trace of Fig. 3(b) for the 8.22V pulse [1]. An initial, single bubble nucleation event occurs at 10.4 μs, evidenced by the rapid drop in conductance. Quasi-periodic bubble nucleation events occur subsequently. (b) Plot of the maximum temperature in the pore as a function of time for the different applied voltage pulses. (c) Plot of the calculated nucleation rate as a function of distance from the center of the pore for 8.22 V applied after times 8 μs, 9 μs, 10 μs, and 10.4 μs. This last time is just before nucleation occurs. The spatial dependence of J was calculated using the temperature distribution at these times. The inset shows the temperature dependence of the surface tension of the liquid-vapor interface of water along the saturation curve [38]. (d) Plot of maximum nucleation rate as a function of time for 8.22 V calculated using the maximum temperature of Fig. 6(b). The inset shows the exquisite sensitivity of the nucleation rate to the temperature [18].
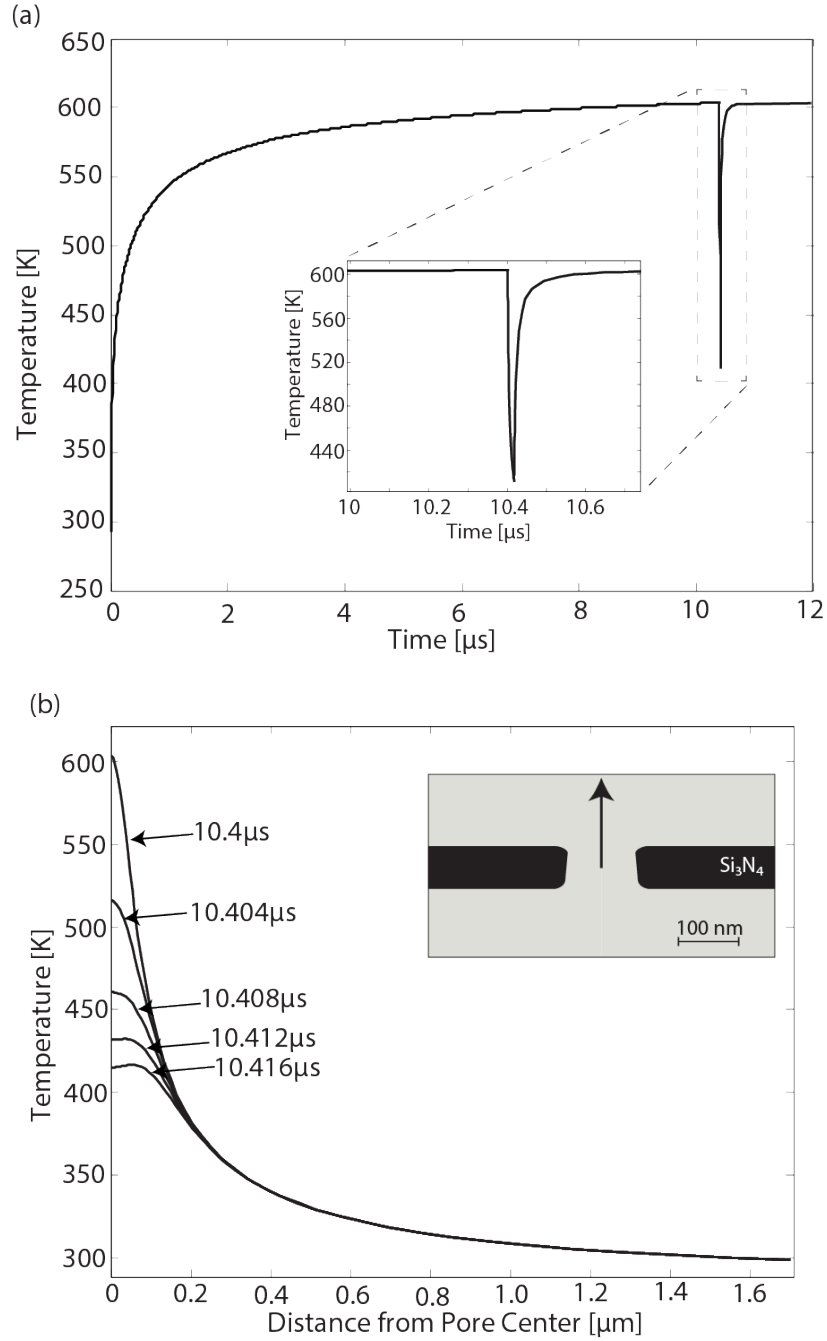
18

FIG. 7 (a) The maximum temperature calculated within the nanopore as a function of time for an applied pulse of 8.22 V. At t = 10.4 µs, the applied voltage is turned off resulting in a drop in peak temperature. After 16 ns, representing the lifetime of the bubble, the pulse is turned back on, and the maximum temperature is seen to quickly return to its original value before the pulse was turned off. (b) The spatial distribution of temperature is plotted along the central axis for different times after the pulse is turned off.
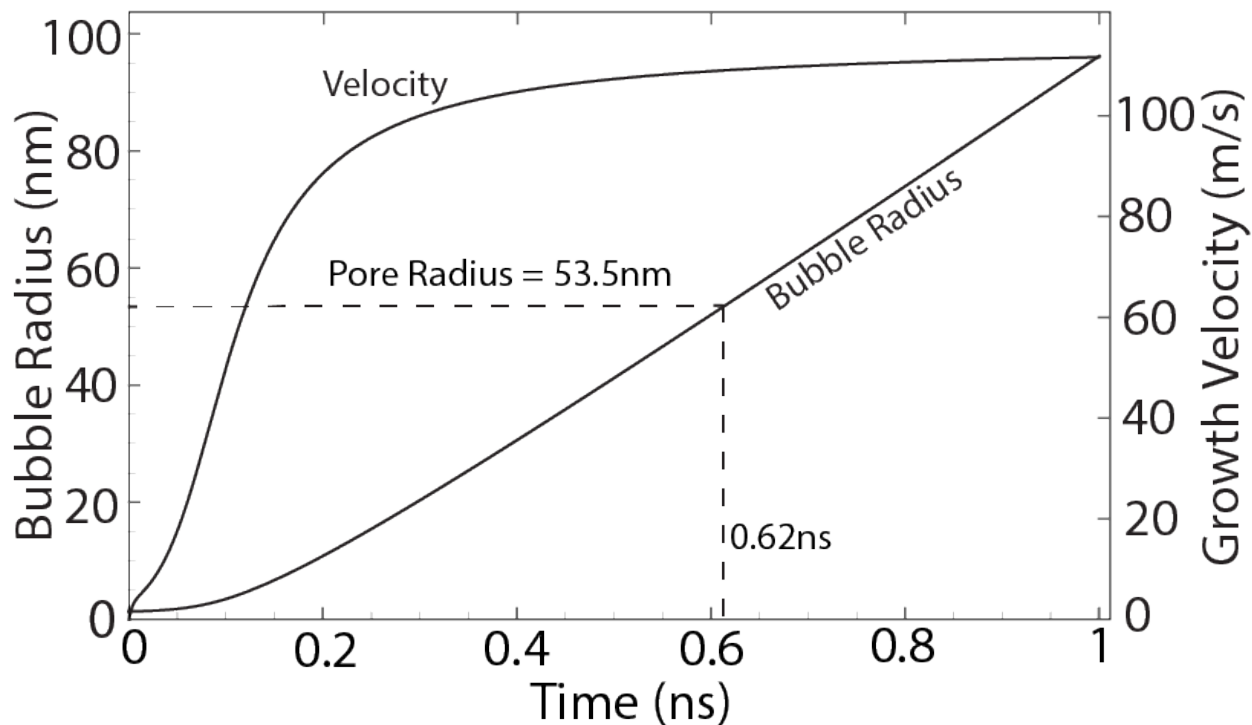
FIG. 8 Bubble radius and velocity as a function of time, calculated using Rayleigh-Plesset dynamics. The bubble is calculated to reach the nanopore radius in 0.62 ns. This compares well with the 1 ns fall time seen in the experimental conductance data presented in Fig. 6(a).